The history of ice-sheet retreat on North America during Termination 5: Implications for the origin of the sea-level highstand during interglacial stage 11

Rebecca L. Parker [a],*, Gavin L. Foster [b], Marcus Gutjahr [c], Paul A. Wilson [b], Stephen P. Obrochta [d], Nathalie Fagel [e], Matthew J. Cooper [b], Agnes Michalik [b], James A. Milton [b], Ian Bailey [a]

[a] Camborne School of Mines, College of Engineering, Mathematics & Physical Sciences, University of Exeter, Penryn Campus, Treliever Road, Penryn TR10 9FE, UK
[b] School of Ocean and Earth Science, University of Southampton, Waterfront Campus, European Way, Southampton SO14 3ZH, UK
[c] GEOMAR Helmholtz Centre for Ocean Research Kiel, Wischhofstraße 1–3, 24148 Kiel, Germany
[d] Graduate School of International Resource Science, Akita University, 1-1 Tegatagakuen Machi, Akita 010-8502, Japan
[e] AGEs, Clay, Geochemistry and Sedimentary Environment, Department of Geology, University of Liège, Allée du Six Août 14, B-4000 Liege, Belgium

ARTICLE INFO

ABSTRACT

Termination (T) 5, ∼424 ka, involved the biggest deglaciation of land-ice mass during the Quaternary. Warming and ice-sheet retreat during T5 led to an exceptionally long period of interglacial warmth known as Marine Isotope Stage (MIS) 11, ∼424–395 ka. A detailed understanding of the history of continental ice-sheet decay during T5 is required to disentangle regional contributions of ice-sheet retreat to sea-level rise (that range between ∼1 and 13 m above present day) and to correct it for glacio-isostatic adjustments (GIA). Yet little is known about the timing and magnitude of retreat during this time of the volumetrically most important continental ice sheet in the Northern Hemisphere, the Laurentide Ice Sheet (LIS). Here we present new authigenic Fe-Mn oxyhydroxide-derived high-resolution records of Pb isotope data and associated rare earth element profiles for samples spanning T5 from Labrador Sea IODP Site U1302/3. These records feature astronomically-paced radiogenic Pb isotope excursions that track increases in chemical weathering of North American bedrock and freshwater routing to the Labrador Sea via Hudson Straits associated with LIS retreat. Our records show that LIS retreat during T5 began 429. 2 ± 7.9 ka (2σ) and likely occurred over a longer timescale (by ∼10 to 5 kyr) than that observed for T2 and T1. They also show that Hudson Bay Ice Saddle collapse (and therefore LIS break-up) occurred ∼419 ± 4.7 ka (2σ), around the same time as best estimates of southern Greenland deglaciation, but ∼12 kyr before LIS deglaciation and the sea-level high-stand associated with the latter half of MIS 11 likely occurred. Our findings therefore highlight that ice-mass loss on North America likely played an important role in the seemingly protracted nature of T5 sea-level rise. A comparison of the deglaciation histories of the LIS and the southern Greenland Ice Sheet during T5, T2 and T1 also demonstrates that the well-constrained history of regional ice-sheet retreat during T1 is not always applicable as a template for older late Pleistocene terminations in GIA modelling.

1. Introduction

Marine Isotope Stage (MIS) 11, ∼424–395 ka, is the longest and warmest interglacial of the last ∼500 kyr (Loutre and Berger, 2003). It is argued by some, from the perspective of astronomically driven insolation, that it also represents the most recent analogue in the geological past for near-future changes in Earth's climate (e.g., Loutre and Berger, 2003; McManus et al., 2003; Dickson et al., 2009) although this is still debated (Rohling et al., 2010). Best estimates of global mean sea-level for MIS 11 lie somewhere between ∼+1 m (Rohling et al., 2010) and ∼+6 to +13 m (e.g. Raymo and Mitrovica, 2012; Dutton et al., 2015) relative to modern sea-level. MIS 11 may therefore feature significant reductions in the volume of both the Greenland (De Vernal and Hilliare-Marcel, 2008; Reyes et al., 2014) and Antarctic (Wilson et al., 2018) ice sheets relative
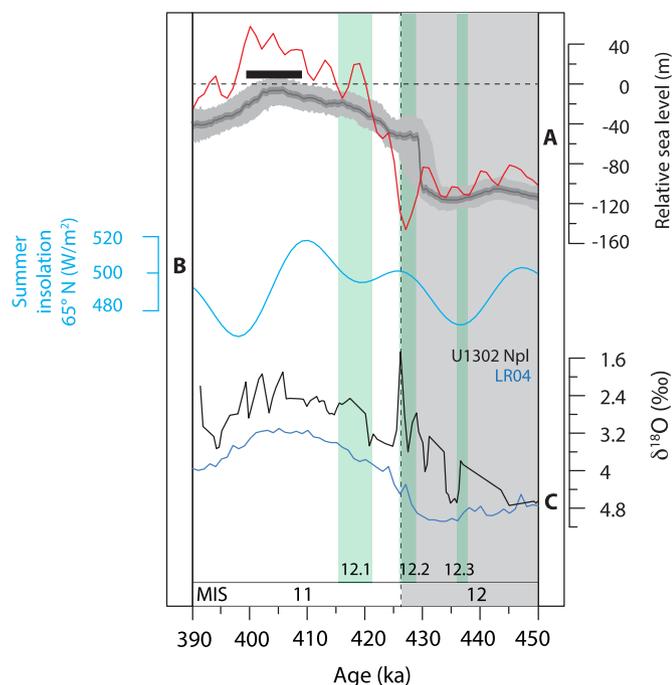
Fig. 1. Palaeoclimate records spanning MIS 12, 11 and Termination 5: (**A**) Red Sea relative sea-level (RSL) record with 95% probability interval for the RSL data (dark grey envelope) and 95% probability interval for the probability maximum (light grey envelope; Grant et al., 2014). Also shown is a benthic foraminiferal-derived seawater-δ^{18}O based RSL record from Ocean Drilling Program (ODP) Site 1123 (red line; Elderfield et al., 2012). The black horizontal bar highlights the timing of $+6$–13 m sea-level reconstructed by Raymo and Mitrovica (2012) during the second half of MIS 11; (**B**) Insolation forcing at 21st June 65°N (Laskar et al., 2004); (**C**) Site U1302/3 planktic *Neogloboquadrina pachyderma* left coiling (Npl) δ^{18}O (black line; Hillaire-Marcel et al., 2011) plotted on age model presented in this study, and the LR04 benthic δ^{18}O stack (blue line; Lisiecki and Raymo, 2005).

to today. The preceding glacial maximum during MIS 12 marked the first time that the British and Fennoscandian ice sheet coalesced during the Quaternary (Toucanne et al., 2009). It also featured a mean global sea-level ~120–130 m below present (Grant et al., 2014), and thus potentially represents the deepest glaciation of the Cenozoic. The MIS 12/11 climate transition, otherwise known as Termination (T) 5 (hereinafter T5), is therefore viewed as the potentially most extreme deglacial climate shift of the Quaternary (Barker et al., 2021).

It is increasingly recognized that not all deglaciations are equal and T5 has been labelled as a 'protracted deglaciation' (Barker et al., 2019) because the full transition in mean global sea-level between MIS 12 and 11 (Rohling et al., 2010; Raymo and Mitrovica, 2012) was seemingly not reached until the second half of MIS 11, ~405 ka, so not until after the second of two weak precession-paced insolation maxima associated with this interglacial was encountered. Palaeoclimate data of MIS 11 are interpreted to record a modest relapse to more glacial-style conditions during the intervening insolation minimum, ~418 ka (Loulergue et al., 2008; Dickson et al., 2009). Global mean sea-level also plateaued at this time before subsequent slow ice-volume reductions led to the MIS 11 sea-level highstand ~405 ka shortly following the second of these insolation maxima (Fig. 1a; Rohling et al., 2010).

A detailed understanding of the history of the decay of continental ice-sheets across T5 is needed to disentangle regional contributions of ice-sheet retreat to this sea-level history. Empirical data of this nature are also required by numerical modellers to correct estimates of MIS 11 sea-level rise accurately for glacial-isostatic adjustment (GIA) for the deformational, gravitational and rotational impacts on sea level driven by cryospheric loading and

unloading of the land and ocean (e.g., Raymo and Mitrovica, 2012; Dendy et al., 2017). It has been shown, for instance, that the accuracy of GIA corrections for global mean sea-level rise during the Last Interglacial (the Eemian) are highly dependent on uncertainties in our understanding of ice-sheet configuration and the duration of deglaciation for the largest ice-mass in the northern hemisphere, the North American Laurentide Ice Sheet (LIS) during the preceding glacial terminations (e.g.; Dendy et al., 2017; Dyer et al., 2021). While strong evidence exists to show that near-complete deglaciation of southern Greenland occurred during MIS 11 by ~418 ka (e.g., De Vernal and Hilliare-Marcel, 2008; Reyes et al., 2014; Hatfield et al., 2016), nothing is known about the history of LIS retreat during T5.

To help address this unknown, we present new high-resolution Fe-Mn oxyhydroxide-derived Pb isotope ratios and rare earth element profiles of 37 samples from Integrated Ocean Drilling Program (IODP) Site U1302/3 in the Northwest North Atlantic on Orphan Knoll that span MIS 12/11 (Fig. 2). The Pb isotope composition of the oxyhydroxide fraction of marine sediments deposited at this site tracks the runoff signal of chemical weathering on North America and Greenland (Crocket et al., 2012; Parker et al., 2022), and has previously been used successfully to track LIS extent in Hudson Bay over the past ~130 kyr (Crocket et al., 2012; Parker et al., 2022).

2. How are changes in Fe-Mn oxyhydroxide-derived Pb isotope ratios from Site U1302/3 related to changes in ice-sheet extent on North America?

The evolution of the Pb isotope composition of seawater bathing Orphan Knoll over the past 25 kyr track changes in the magnitude of chemical weathering and solute runoff associated with LIS extent in the Hudson Bay region of North America (Crocket et al., 2012; Parker et al., 2022). This evolution can be tracked by analysing the Pb isotope composition of the Fe-Mn oxyhydroxide fraction of marine sediments deposited at IODP Site U1302/3 (Fig. 3). Trends in the Pb isotope composition of the corresponding detrital fraction are decoupled from this seawater signal (Crocket et al., 2012; Parker et al., 2022). Instead they reflect changes in the source(s) of terrigenous inputs associated with iceberg-rafting, bottom currents and aeolian dust deposition, which can also be derived from further afield than the dissolved Pb runoff responsible for setting the Pb isotope composition of seawater bathing Orphan Knoll.

The unradiogenic Pb isotope signature of seawater bathing Orphan Knoll during the Last Glacial Maximum (LGM; Fig. 2a) fingerprints a reduction in chemical weathering and runoff on North America under a spatially extensive and largely cold-based LIS, and a dominance of relatively unradiogenic North American aeolian dust and Mid-Atlantic Ridge Pb isotope signals (Crocket et al., 2012; Parker et al., 2022). This unradiogenic signature is also amplified by a sluggish Labrador Current compared to modern, which, given the particle-reactive nature and short seawater residence time of Pb, would have reduced the supply of radiogenic Pb to U1302/3 from inner parts of the Labrador Sea during the LGM (Parker et al., 2022).

Highly radiogenic millennial-scale excursions in Site U1302/3 authigenic Pb isotope data associated with Last Glacial Heinrich events (orange star in Fig. 3a) are suggested to represent the measurement of "pre-formed" coatings of detrital grains in H-layers rafted to Orphan Knoll in icebergs sourced from Hudson Bay rather than a record of contemporaneous seawater composition (Crocket et al., 2012). Previously published Site U1302/3 authigenic Pb isotope data feature longer-term orbital-scale radiogenic excursions during T2 (from ~130 ka, Fig. 3b; Parker et al., 2022) and T1 (from ~20 ka, Fig. 3a; Crocket et al., 2012), which have been
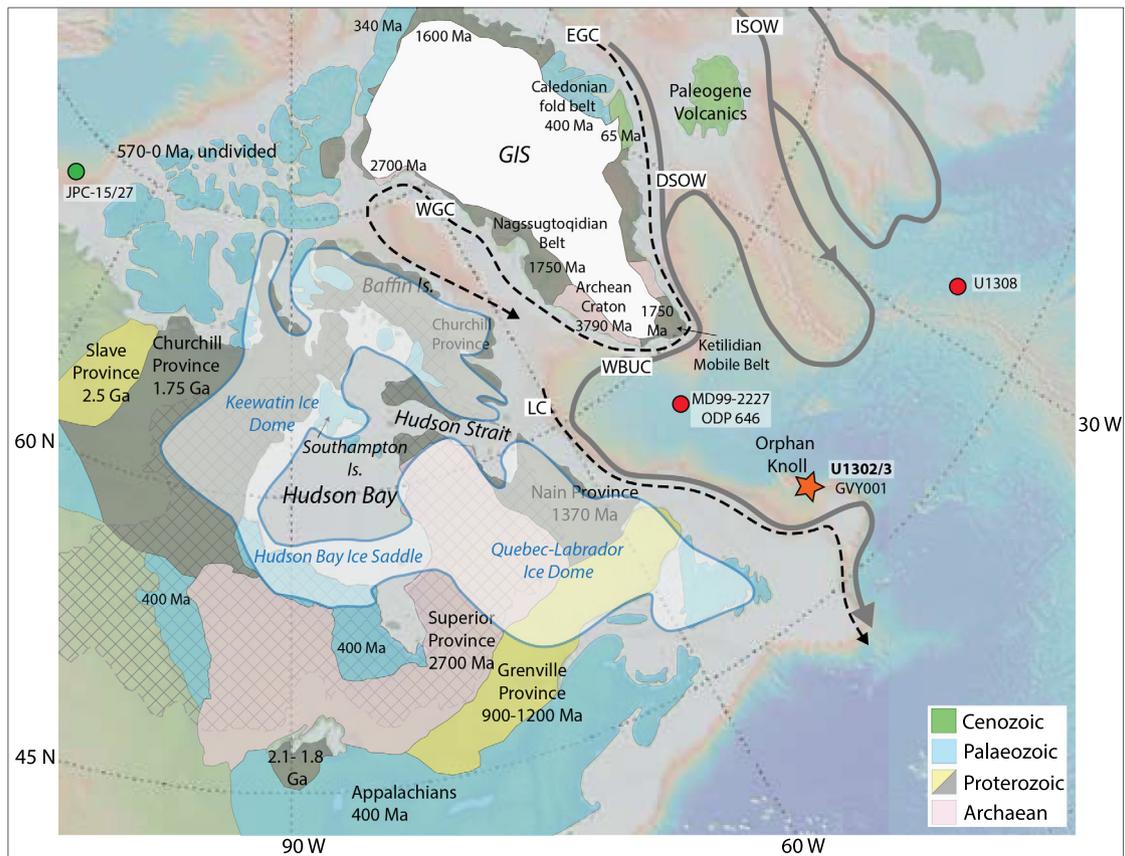
Fig. 2. Map showing location of IODP Site U1302/3 (larger orange star), other sites discussed in the text (e.g., JPC-15/27; green circle), relevant surrounding cratonic (bedrock) geology, and schematic of the spatial extent of the Keewatin and Quebec-Labrador ice domes and Hudson Bay Ice Saddle ∼8.5 ka (Lochte et al., 2019). Geology of North America and Greenland redrawn from Parker et al. (2022) and White et al. (2016). GIS = modern Greenland Ice Sheet. Grey hatched region denotes modern area of watershed drainage into Hudson Bay and its straits (Natural Resources Canada, 2006). Arrows denote simplified paths of key modern deep (solid grey) and surface (dashed grey) ocean currents/bottom-water pathways relevant to this study (redrawn from Blake-Mizen et al., 2019). DSOW – Denmark-Scotland Overflow Water. EGC = East Greenland Current. ISOW = Iceland-Scotland Overflow Water. WBUC = Western Boundary Undercurrent. LSW = Labrador Sea Water. WGC = West Greenland Current.

attributed to increased flux of radiogenic solute to the ocean following the onset of LIS retreat and its change from a largely cold- to warm-based ice-sheet (Crocket et al., 2012; Parker et al., 2022). This radiogenic signal would have been transmitted to U1302/3 via the Labrador Current and Western Boundary Undercurrent (WBUC; Fig. 2). Two main processes have been proposed to explain its origin: 1) incongruent weathering of highly reactive, only slightly chemically weathered (hereafter termed fresh) glacial debris, exposed following LIS retreat (Crocket et al., 2012) and/or, (2) changes in Pb provenance through enhanced sourcing and congruent weathering of fresh radiogenic North American Superior Province (SP) cratonic material (Fig. 4; Blaser et al., 2020; Parker et al., 2022). We note that the SP is the only regional continental source with Pb isotope ratios high enough to explain the values recorded in the authigenic fraction of U1302/3 deglacial sediments through a change in Pb provenance (Fig. 4). The relative importance of these two processes in controlling the Pb isotope composition of solute flux is debated (e.g., Crocket et al., 2012; Dausmann et al., 2019; Süfke et al., 2019, 2022). Their relative roles in controlling changes in authigenic Pb isotope records from U1302/3 have recently been discussed extensively in Parker et al. (2022) where it was concluded that if incongruent weathering influences the Pb isotope composition of seawater bathing Orphan Knoll during LIS deglaciation its role is likely to have been subordinate to that of changes in Pb provenance. Regardless of the mechanisms involved, the radiogenic deglacial signals recorded in authigenic Pb isotope data from U1302/3 provide important insights into the timescales of LIS retreat during terminations.

The deglacial sequence of LIS retreat during T1 has been mapped out in detail using geomorphology, stratigraphy and radiocarbon dating (e.g., Dyke et al., 2002; Dalton et al., 2020). These data show that the onset of the orbital-scale increase in radiogenic values in U1302/3 Pb isotope records at ∼20 ka coincides with the earliest stages of elevated freshwater runoff associated with LIS retreat on North America (in Long Island Sound, Connecticut; Dalton et al., 2020; Crocket et al., 2012; Parker et al., 2022). It also shows that peak radiogenic Pb isotope compositions in the Orphan Knoll record for T1 were reached ∼2 kyr following the collapse of the Hudson Bay Ice Saddle between the Keewatin and Labrador domes (∼8.7–8.15 ka; Dalton et al., 2020; Brouard et al., 2021). A similar timing for Hudson Bay Ice Saddle collapse has recently been inferred from authigenic Pb isotopic records recovered from sediments deposited proximal to the Arctic Mackenzie Delta (Fig. 3a; Süfke et al., 2022).

The relatively sudden return to late Holocene-like values in these Arctic records from ∼8.5 ka is argued to show that freshwater routing of a highly radiogenic Pb signal into the Arctic Ocean from a disintegrating LIS was cut off shortly after Hudson Bay Ice Saddle collapse (the green JPC 15/27 record in Fig. 3a; Süfke et al., 2022). Labrador Dome break-up did not occur for another ∼3 kyr (at ∼5.7 ka), after which glaciation of northeast North America was mainly restricted to the Canadian Arctic Archipelago (Dalton et al., 2020). The slower paced decay towards late Holocene-like unradiogenic values recorded in authigenic Pb isotope records from U1302/3 (which were not attained until ∼3 ka; Fig. 3a, b), therefore likely highlights that freshwater runoff associated with these
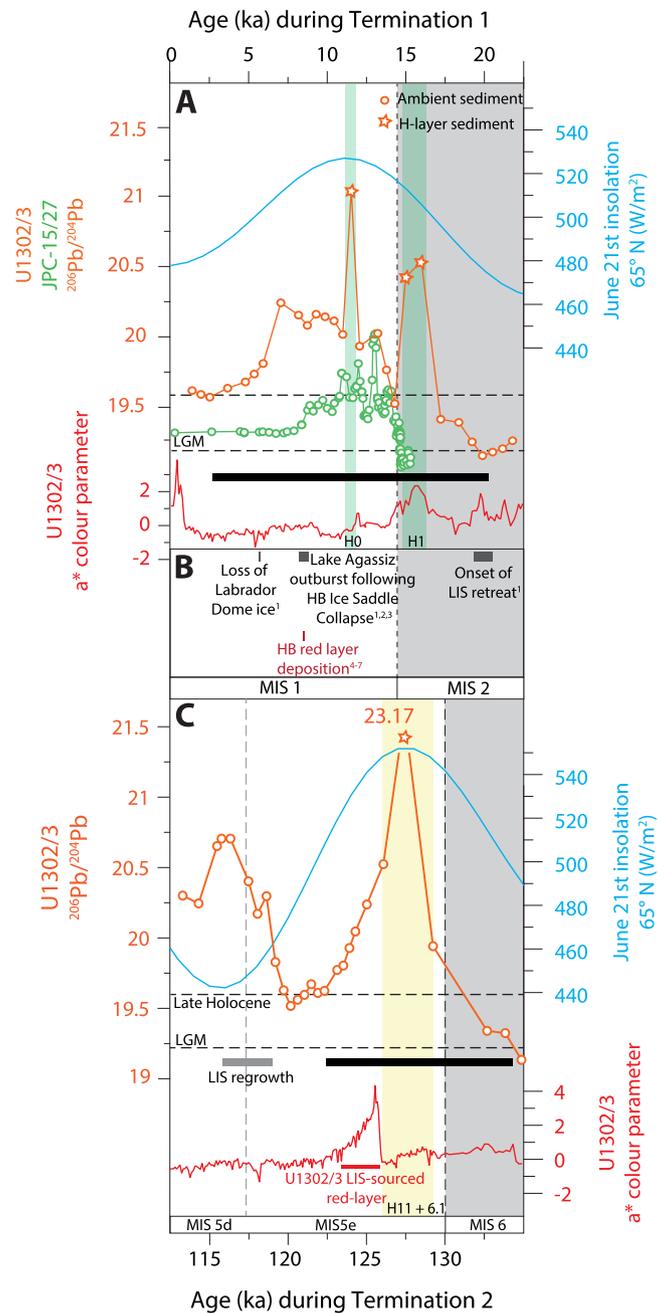
Fig. 3. The evolution of the Pb isotope composition of authigenic Fe-Mn oxyhydroxides from IODP Site U1302/3 during (**A**) Termination 1(T1) associated with (**B**) major events of Laurentide Ice Sheet (LIS) retreat and (**C**) Termination 2 (T2). Pb isotope composition of authigenic Fe-Mn oxyhydroxides from Site JPC-15/27 (Süfke et al., 2022) shown by open green circles in (A) offset from true y-axis values for clarity. Horizontal black bars highlight the inferred duration of enhanced supply of a dissolved radiogenic weathered signal following LIS retreat during T2/T1. Light grey horizonal bar in (C) highlights the duration of LIS regrowth associated with the onset of the Last Glacial Cycle (Parker et al., 2022). Dark grey horizontal bars and associated superscript numbers in (B) highlight timing of major events that characterise LIS retreat during T1, whereby 1 = Dalton et al. (2020; ^{14}C and OSL ice margin chronology), 2 = Brouard et al. (2021; marine and terrestrial ^{14}C dates, geomorphic and varve records), 3 = Margold et al. (2018; ice stream mapping), 8 = Dyke et al., 2002; ^{14}C ice margin chronology). Also shown is timing of the deposition of a red layer in Hudson Bay (HB) during T1 (4 = Barber et al. (1999), 5 = Lajeunesse and St-Onge (2008), 6 = Jennings et al. (2015), 7 = Lochte et al. (2019), argued to be the product of extensive deglaciation of the Hudson Bay region following the collapse of the HB Ice Saddle and the final outburst of glacial Lake Agassiz-Ojibway (Carlson et al., 2008). A similar red layer was deposited in the Labrador Sea during T2 (see red horizontal bar associated with peak in a* sediment colour in (C), argued to document a large glacial outburst flood from a precursor to glacial Lake Agassiz-Ojibway (Nicholl et al., 2012). Solid orange circles/stars in (C) = Parker et al. (2022); open orange circle/stars in (A) = Crocket et al. (2012). Cold (warm) Marine Isotope Stages (MIS) shown by vertical light grey (white) bars. Heinrich (detrital) layers preserved in both the Labrador Sea (identified using U1302/3 core-scanning-derived XRF Ca/Sr ratios by Channell et al. (2012)) and subpolar North Atlantic sediments (Hodell et al., 2008) shown by labelled vertical light green bars. Labelled vertical light-yellow bars highlight Heinrich-like detrital layers where deposition was restricted to the Labrador Sea (Channell et al., 2012; Hodell et al., 2008). Horizontal dashed lines in (A) and (C) highlight average Pb isotopes values for the LGM and late Holocene. Blue insolation forcing curves for 21st June 65°N (Laskar et al., 2004) are also shown for T1 (in A) and T2 (in C).

final stages of LIS retreat continued to be routed to Orphan Knoll via Hudson Straits. The collapse of the Hudson Bay Ice Saddle caused the final outburst of glacial Lake Agassiz-Ojibway south of Hudson Bay (Brouard et al., 2021) and the deposition of a red

detrital marker bed in Hudson Straits sediments (Fig. 3a,b; e.g., Jennings et al., 2015). A similar red (hematite-rich) detrital layer has been found in sediments deposited at Site U1302/3 during T2 (Fig. 3c; Nicholl et al., 2012), which correlates with peak radiogenic
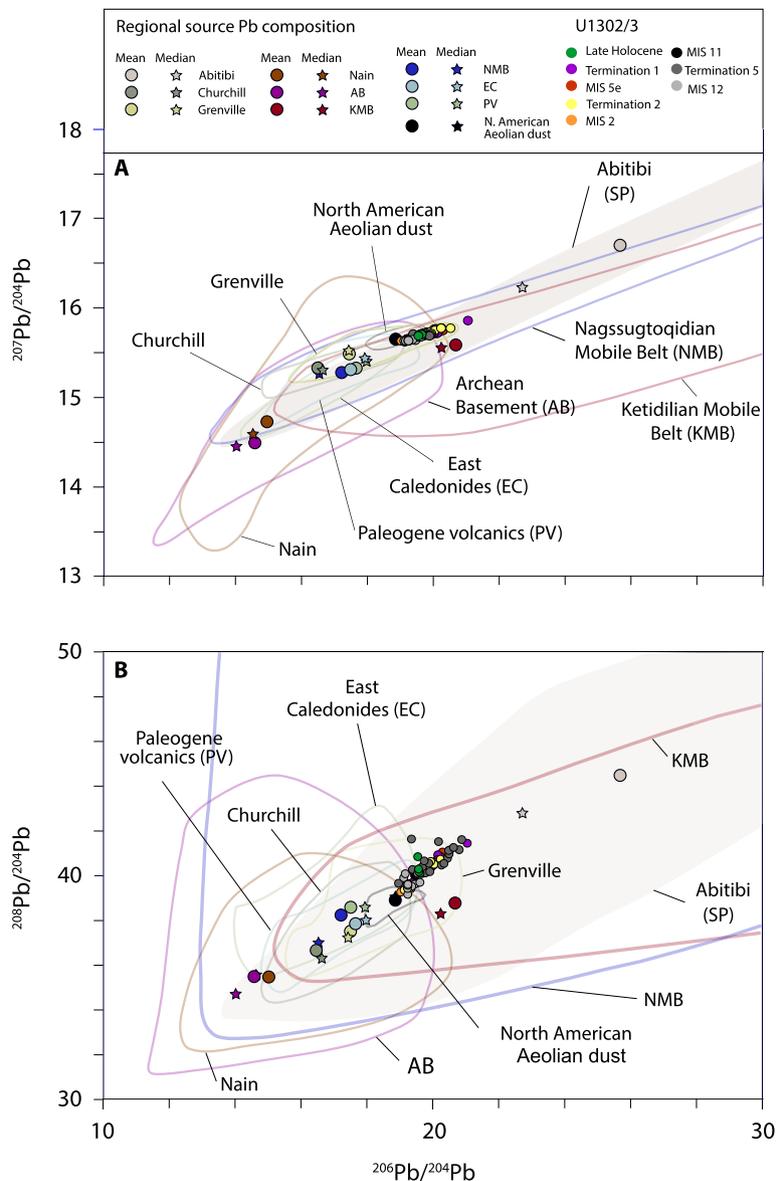
Fig. 4. The Pb isotope composition of cratonic bedrock adjacent to Orphan Knoll Site U1302/3: (A) $^{206}Pb/^{204}Pb$ vs. $^{207}Pb/^{204}Pb$ and (B) $^{206}Pb/^{204}Pb$ vs. $^{207}Pb/^{204}Pb$. Redrawn from Parker et al. (2022), which in turn was based on a whole rock data compilation by Fagel et al. (2002) supplemented by additional datasets. The Pb isotopic composition of the authigenic Fe-Mn oxyhydroxide fraction of U1302/3 sediments is also shown for the late Holocene (green circles), Termination 1 (purple circles), MIS 5e (red circles), Termination 2 (yellow circles) and MIS 2 (orange circles). See Fig. 2 for craton locations. We defined the average weathering Pb isotope signal of each source following Parker et al. (2022, and references therein) by using the mean and median of the whole-rock data available for each craton. The degree of disparity between the mean and the median can be used as a first-order estimate of uncertainty in our understanding of each end-member's average Pb isotope composition.

values in the authigenic Pb isotope record from this site ∼126 ka (Fig. 3c; Parker et al., 2022). This detrital red layer is associated with increased values in an a* colour reflectance record of U1302/3 sediments (Fig. 3c) and is interpreted to reflect extensive deglaciation of the Hudson Bay region following a last deglacial-like collapse of an LGM-like Hudson Bay Ice Saddle and a subsequent Lake Agassiz-like glacial outburst flood (Nicholl et al., 2012).

The time from which authigenic Pb isotope data from Orphan Knoll first exhibit late Holocene-like values (e.g., ∼19.6 $^{206}Pb/^{204}Pb$, ∼15.7 ∼$^{207}Pb/^{204}Pb$, and ∼40.0 $^{208}Pb/^{204}Pb$) provides a marker for the total loss of the LIS during deglaciation. The Pb isotope composition of seawater bathing Orphan Knoll from this time represents a new interglacial equilibrium reached following deglaciation of North America, but in a world in which Greenland remained largely glaciated (Colville et al., 2011). This observation has important implications for the interpretation of older interglacial U1302/3 authigenic Pb isotope data. This is because, in contrast to the late Holocene, near-complete deglaciation of southern Greenland has been reconstructed for MIS 11 from ∼418 ka using the magnetic properties (Hatfield et al., 2016) and Sr-Nd-Pb isotope compositions (Colville et al., 2011; Hatfield et al., 2016; Reyes et al., 2014) of Precambrian Greenland (PG)-sourced silt discharged to Eirik Drift sediments via the WBUC during southern Greenland Ice Sheet (sGIS) retreat. A subsequent increase in the solute flux of the chemically weathered products of southern Greenland to Orphan Knoll via the WBUC (Fig. 2) should be registered by a change in the Pb isotope composition of waters bathing U1302/3 because solute flux from this region can be differentiated from that derived from the North American SP on the basis of its distinct (less radiogenic) lower mean Pb isotope composition (see the Ketidilian Mobile Belt (KMB), Nagssugtoqidian Mobile Belt (NMB) and Archean Block (AB) terranes in Fig. 4; Parker et al., 2022).

The amount of summer insolation received at high northern latitudes plays a major role in determining the timing and duration

of northern hemisphere deglaciation (Raymo, 1997; Carlson et al., 2008). The LIS is, for instance, argued to have retreated faster during T2 than it did during T1 as a result of greater boreal summer insolation forcing (Carlson et al., 2008). This suggestion is consistent with the evolution of orbital-scale changes in radiogenic authigenic values in U1302/3 Pb isotope data (Fig. 3). Insolation forcing during T5 across the MIS 12/11 transition is weaker (by $\sim$20 and 40 W m^2) than during T1 and T2, respectively (compare June 21st insolation time series in Fig. 1b and Fig. 3a, c). Maximum values in insolation were also not reached until the second of two weak precessional-paced maxima associated with MIS 11 (Fig. 1b), 17 to 14-kyr later than maximum values in insolation were reached during MIS 5e and the Holocene, respectively.

In this study, we use a new high-resolution authigenic Pb isotope record from Site U1302/3 and a lower-resolution detrital Pb isotope record to track LIS retreat during T5 with respect to this insolation history. In doing so we address the following questions: (1) When did LIS retreat begin during T5? (2) What is the relationship between the timing of Hudson Bay Ice Saddle collapse and the two weak precessional-paced maxima in insolation associated with MIS 11? (3) By what time was LIS deglaciation complete during MIS 11? (4) Does evidence also exist in U1302/3 authigenic Pb isotope data for deglaciation of southern Greenland during MIS 11?

3. Methods

3.1. Site description, sampling and age model

IODP Site U1302 (50° 10′N, 45° 38.3′W, water depth $\sim$3560 m) and Site U1303 (50° 12.4′N, 45°41.2′W, water depth $\sim$3520 m) are located $\sim$3 nautical miles apart on the SE flank of Orphan Knoll within the Labrador Sea (Channell et al., 2006). The similarity of strata between the two sites has been used to create continuously spliced composite records of changes in bottom-water Pb isotope compositions over the past $\sim$130 kyr (Crocket et al., 2012; Parker et al., 2022).

To reconstruct the Pb isotope composition of bottom waters bathing Site U1302/3 during T5, we determined the authigenic Fe-Mn oxyhydroxide fraction of 5-c m^3 samples (n = 37) taken every 10-20 cm between 59.25-63.51 meters composite depth, mcd (Expedition 303 Scientists, 2006). These samples were also used to determine selected elemental concentrations and ratios of the seawater derived Fe-Mn oxyhydroxide fraction. The age model for our T5 record is based on tuning the U1302/3 relative paleointensity (RPI) record (Channell et al., 2012) spanning our target interval to the HINAPIS-1500 RPI stack (Xuan et al., 2016) on its LR04 benthic δ^{18}O-based age model (Lisiecki and Raymo, 2005) using the depth modelling routine *Undatable* (Lougheed and Obrochta, 2019). We followed a similar procedure to update the T2 and T1 age models for our study site (see Supplementary Information, SI, Section S1). We then used the age-model uncertainties generated by *Undatable* (Figs. S1 and S2) to compare changes in our authigenic Pb isotope datasets from Site U1302/3 to changes in orbital insolation during T5, T2 and T1.

3.2. Pb isotope analysis

We generated new authigenic Pb isotope and rare earth element (REE) data for the MIS 12–11 transition during T5 ($\sim$440–395 ka), following the procedure used by Parker et al. (2022). All sample processing and laboratory analyses were conducted at the University of Southampton. Briefly, Pb was extracted from the authigenic Fe-Mn oxyhydroxide fraction of sediments from each sample closely following Blaser et al. (2016). Dried, homogenized sediment samples were exposed to a leaching solution (mixture of 3 mM Na-EDTA, 5 mM hydroxylamine-hydrochloride, 1.5% acetic

acid and buffered to pH 4 using 0.04M NaOH) to extract the authigenic fraction. The leached solution was then screened on a Thermo Scientific X-Series 2 ICP-MS to ensure adequate quantities of Pb were extracted for column chemistry, before being separated from the matrix using Eichrom AG1-X8 200-400 mesh anion exchange resin (Strelow, 1978). Pb procedural blanks for Fe-Mn oxyhydroxide and detrital fraction samples were estimated at 0.028 ng (n = 14) and 0.001 ng Pb (n = 1), respectively. A set of 8 detrital (residual fraction) samples were also prepared for Pb isotope analysis by MC-ICP-MS. All samples were analyzed in the same run used to generate the Pb isotope data presented in Parker et al. (2022). We employed the double-spike methodology from Taylor et al. (2015) to correct for instrumental mass fractionation. Authigenic Pb masses ranged from $\sim$36 to 198 ng. The reproducibility of the Pb isotope ratio measurements were estimated based on 17 analyses of the SRM NBS 981 measured throughout 2018–2020. Over this analytical period, measured ratios and uncertainties (2 S.D.) were as follows relative to the values of Baker et al. (2004) as shown in parentheses: ^{206}Pb/^{204}Pb = 16.9424 ± 0.00044 (16.9420 ± 0.0001), ^{207}Pb/^{204}Pb = 15.4982 ± 0.001 (15.5010 ± 0.0001) and ^{208}Pb/^{204}Pb =36.7182 ± 0.0028 (36.730 ± 0.0002). To monitor reproducibility of Pb isotope measurements, further, an internal replicate of an authigenic Fe-Mn oxyhydroxide sample from Site U1302/3 was measured in every run (n = 5) and underwent full sample preparation starting with leaching of a sample aliquot. This sample yielded average ratios and uncertainties (2 S.D.) of ^{206}Pb/^{204}Pb = 19.1946 ± 0.0004, ^{207}Pb/^{204}Pb = 15.6341 ± 0.0009 and ^{208}Pb/^{204}Pb =3.5237 ± 0.0021.

3.3. Rare and trace elements analysis

Trace element concentrations of the Fe-Mn oxyhydroxide fraction stock solutions were generated following the methods described in Parker et al. (2022) and were used to evaluate the fidelity of our MIS 12–11 seawater Pb isotope data. Aliquots were prepared for analysis on a Thermo Scientific X-Series 2 ICP-MS at the School of Ocean and Earth Science, University of Southampton. Measurements were calibrated using the same suite of international rock standards and in-house and international reference materials outlined in Parker et al. (2022). REE concentrations of samples were normalised relative to the REE profile of the Post-Archean Australian Shale (PAAS; Taylor and McLennan, 1985) and a number of ratios of PAAS-normalised measurements were calculated following Martin et al. (2010) and Blaser et al. (2016, 2019; also see Parker et al. (2022)).

4. Results and discussion

4.1. New MIS 12/11 Pb isotope data from Site U1302/3

In Fig. 5 we present the first high-resolution records of authigenic Fe-Mn oxyhydroxide-derived Pb isotopes from Site U1302/3 that span the transition between MIS 12/11 during T5, and compare these with equivalent records spanning MIS 6 to 5e (T2; Parker et al., 2022) and MIS 2 to 1 (T1; Crocket et al., 2012). The Pb isotope zones for MIS 6/5e and MIS 2/1 shown in Fig. 5 (and labelled with Greek letters $\alpha - \delta$ and $\eta - \iota$) are the same as those used by Parker et al. (2022) to highlight important features in the evolution of the Pb isotope composition of Orphan Knoll seawater during these times. Here we extend these Pb isotope zones back to MIS 12 (κ-μ) to aid comparison of the deglacial trends in these U1302/3 authigenic datasets for T5, T2 and T1.

Our new MIS 12/11 records show that detrital carbonate layers deposited at our study site during MIS 12 (12.3 and 12.2) and T5 (12.1) are associated with millennially-paced excursions to highly radiogenic values comparable to those observed for detrital layers
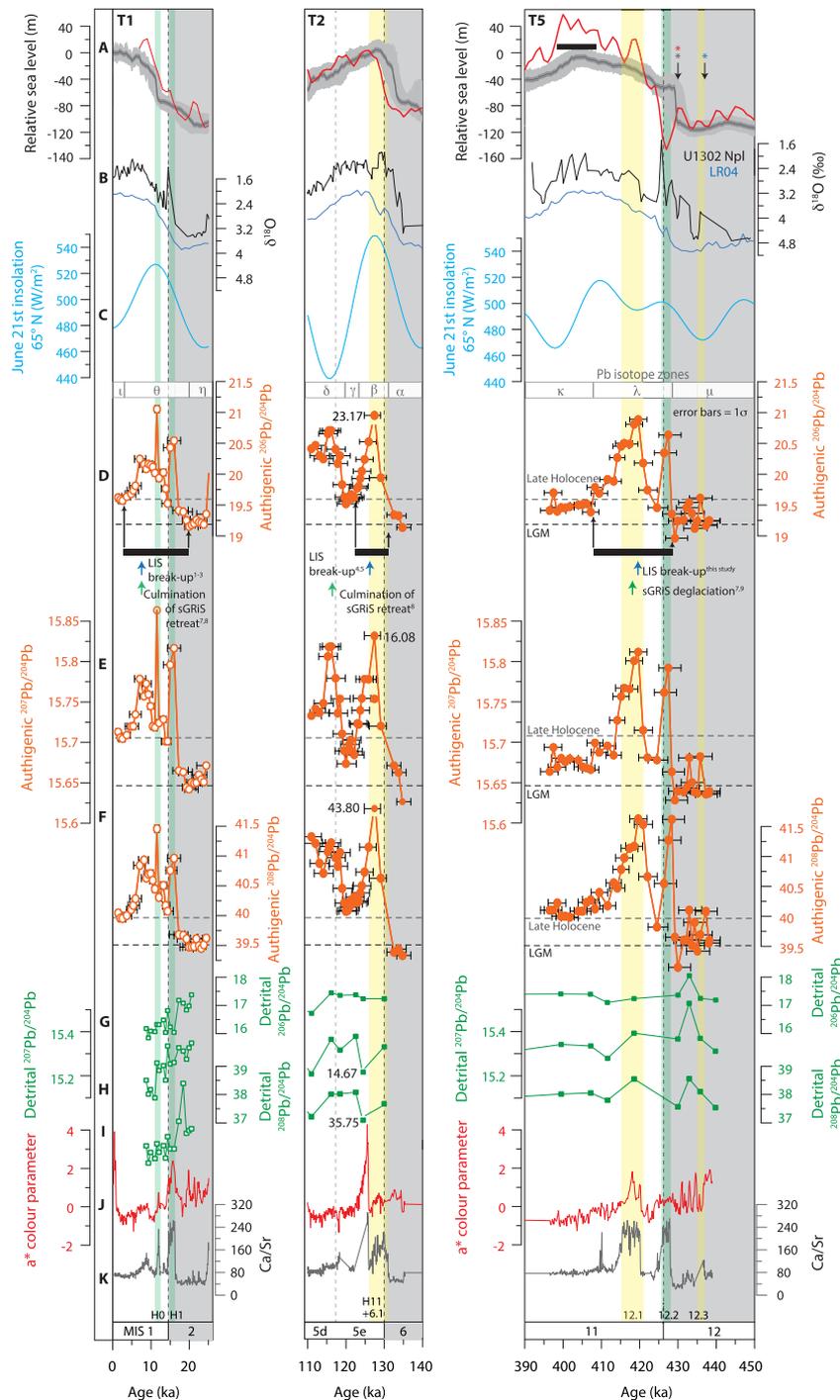
Fig. 5. Comparison of palaeoceanographic and palaeoclimate records during Termination (T) 5, T2 and T1: (**A**) Red Sea relative sea-level (RSL) record with 95% probability interval for the RSL data (dark grey envelope) and 95% probability interval for the probability maximum (light grey envelope; Grant et al., 2014). Also shown is a benthic foraminiferal-derived seawater-δ^{18}O based RSL record from ODP Site 1123 (red line; Elderfield et al. (2012). The black horizontal bar highlights the timing of +6–13 m sea-level reconstructed by Raymo and Mitrovica (2012) during the second half of MIS 11; the black vertical arrows indicate timing of T5 according to Grant et al. (2014; grey asterisk), Cheng et al. (2012; red asterisk), Regattieri et al. (2016; blue asterisk); (**B**) Site U1302/3 planktic δ^{18}O (black line; Hillaire-Marcel et al., 2011) and the LR04 benthic δ^{18}O stack (blue line; Lisiecki and Raymo, 2005); (C) Insolation forcing at 21st June 65°N (W/m^2; Laskar et al., 2004); Pb isotope ratios of authigenic Fe-Mn oxyhydroxides from U1302/3: (**D**) ^{206}Pb/^{204}Pb; (**E**) ^{207}Pb/^{204}Pb; (**F**) ^{208}Pb/^{204}Pb (T1 and T2, Parker et al., 2022; T5, this study) with 1σ age error bars (see SI File Section S1); Pb isotope ratios of detrital sediment fraction: (**G**) ^{206}Pb/^{204}Pb; (**H**) ^{207}Pb/^{204}Pb; (**I**) ^{208}Pb/^{204}Pb ratios of Site U1302/3 (T1 and T2, Parker et al., 2022; T5, this study). "Detrital" refers to the full digestion of the authigenic-free fraction of marine sediment; (**J**) a* colour reflectance parameter highlighting red detrital sediment layers; (**K**) XRF Ca/Sr ratios (counts/counts) from U1302/3 (Channell et al., 2012). MIS cold (warm) stages are shown by vertical light grey (white) bars. Heinrich-like (detrital carbonate) layers preserved in both the Labrador Sea (identified using core-scanning-derived XRF Ca/Sr ratios by Channell et al., 2012) and subpolar North Atlantic sediments (Hodell et al., 2008) are shown by labelled vertical light green bars. Labelled vertical light-yellow bars highlight Heinrich-like detrital layers where deposition was restricted to the Labrador Sea (Channell et al., 2012; Hodell et al., 2008). Horizontal dashed lines in (D) (E) and (F) highlight average Pb isotopes values at U1302/3 for the late Holocene and Last Glacial Maximum (LGM). Horizontal black bars and associated arrows in (D) highlight intervals over which we infer enhanced supply of dissolved radiogenic weathered material from the Superior Province craton following Laurentide Ice Sheet (LIS) retreat in the Hudson Bay region during T5, 2 and 1. Blue arrows highlight inferred timings of LIS break-up (Hudson Bay Ice Saddle collapse) during T1 (1 = Carlson et al., 2008; 2 = Dalton et al., 2020; 3 = Brouard et al., 2021), T2 (4 = Nicholl et al., 2012; 5 = Parker et al., 2022) and T5 (this study). Green arrows highlight inferred culmination of southern Greenland Ice Sheet retreat during T1 (7 = Hatfield et al., 2016; 8 = Colville et al., 2011), T2 (8 = Colville et al., 2011). The Greenland Ice Sheet experienced near-complete deglaciation during T5, from ∼418 ka (9 = Reyes et al., 2014; 7 = Hatfield et al., 2016). Greek symbols θ-ι labelled in (D) correspond to Pb isotope data zones referred to in main text.

deposited in the Labrador Sea during Heinrich events of the Last Glacial (see Pb data within yellow and green bars in Fig. 5d–f; Parker et al., 2022; Crocket et al., 2012; Kurzweil et al., 2010). At the orbital scale, these records also demonstrate that the general evolution of authigenic Pb isotope data from U1302/3 for T5 was similar to that observed for T2 and T1– all three Pb isotope ratios (^{206}Pb/^{204}Pb, ^{207}Pb/^{204}Pb and ^{208}Pb/^{204}Pb) are most unradiogenic during MIS 12 (Pb isotope zone μ in Fig. 5d–f) and most radiogenic during T5 and the early stages of MIS 11 (Pb isotope zone λ in Fig. 5d–f) before decaying to intermediate values from ∼416 ka. Prior to ∼429 ka, MIS 12 is characterized by LGM-like Pb isotope values, but only intermittently and overall values vary between ∼19–19.4 for ^{206}Pb/^{204}Pb, ∼15.63–15.67 for ^{207}Pb/^{204}Pb and ∼39.5–40.1 for ^{208}Pb/^{204}Pb (Pb isotope zone μ in Fig. 5d–f). All Pb isotope ratios become progressively more radiogenic from ∼429 ka during T5 (and shift from ∼19.0 to 20.9 for ^{206}Pb/^{204}Pb, ∼15.6 to 15.8 for ^{207}Pb/^{204}Pb and ∼39.2 to 41.6 for ^{208}Pb/^{204}Pb; Pb isotope zone λ in Fig. 5d–f). Excluding H-events, the magnitude of change in these records during this time is comparable to the evolution of the authigenic Pb isotope data from our study site for T2 and T1 (compare Pb isotope zones $\mu - \kappa$ for MIS 12/11 with those for MIS 6/5e ($\alpha - \gamma$) and MIS 2/1 ($\eta - \iota$) in Fig. 5d–f). Late Holocene-like Pb isotope compositions (∼19.6 ^{206}Pb/^{204}Pb; ∼15.7 ^{207}Pb/^{204}Pb; ∼40.0 ^{208}Pb/^{204}Pb), observed after full deglaciation of the LIS, are not recorded in all three authigenic Pb isotope ratios at the same time; they are, for example, first recorded in ^{207}Pb/^{204}Pb from ∼413 ka, in ^{206}Pb/^{204}Pb from ∼407 ka and from ∼405 ka in ^{208}Pb/^{204}Pb (Fig. 5d–f). The duration over which authigenic Pb isotope data from U1302/3 during T5 are characterised by highly radiogenic values ranges between 16.0 ± 9.2 ka (2σ) and 24.2 ± 9.0 kyr (2σ), which is potentially longer than during T1 (∼17.3 ± 4.5 kyr, 2σ) and T2 (∼12.6 ± 8.0 kyr, 2σ; compare Pb isotope zones λ, β and θ in Fig. 5d). Our detrital fraction Pb isotope records show different absolute ratios (e.g., ∼17–18 for ^{206}Pb/^{204}Pb) and contrasting temporal trends across MIS 12 and 11 to those recorded by our authigenic records (compare Fig. 5g–i to 5d–f).

4.2. Fidelity of the U1302/3 authigenic Fe-Mn signal as a record of Labrador Sea seawater Pb isotope composition

To determine the fidelity of our new seawater Pb isotope records for MIS 12 and 11, we checked for the possible release of non-seawater-derived Pb from the detrital sediment fraction. We did this by employing the same series of tests used to examine the fidelity of authigenic Pb isotope data generated from U1302/3 for the past ∼130 kyr (Parker et al., 2022). These tests were as follows: (1) examination of detrital and authigenic Pb isotope trends for evidence of covariance, (2) evaluation of REE data to identify what material was leached (Haley et al., 2004; Martin et al., 2010) and, (3) comparison of Al/Nd, Al/Th and Al/Pb ratios of the authigenic and detrital fractions of our samples and abyssal ocean Fe-Mn crusts (Gutjahr et al., 2007).

An ongoing debate in the literature concerns the extent to which authigenic Nd isotope records from the North Atlantic are strongly influenced by boundary exchange (in situ silicate weathering at the seafloor) and thus that they do not represent a primary record of watermass provenance and mixing (e.g., Du et al., 2020; Abbott et al., 2022; Pöppelmeier et al., 2022). Based on analysis of samples from equatorial Southeast Asia and numerical simulations, Chen et al. (2023) recently argued that pre-anthropogenic Pb isotope signatures in seawater could be affected by similar processes. Yet, their study region accounts for 2/3s of the global fluvial sediment flux to the ocean. It is influenced by high erosion rates and heavy rainfall with twice the oceanic Pb flux than that originating from North America (Chen et al., 2023). Their findings may therefore not be a good analogy for the Orphan Knoll environment.

It has also been recently shown that changing composition of lithogenic sediments during glacial terminations can play a leading role setting the Nd isotope composition of the authigenic fraction of North Atlantic marine sediments through either benthic flux and/or silicate leaching by porewaters (Abbott et al., 2022). Yet, the absence of covariance between our authigenic and detrital Pb isotope records, as well as the pronounced offset in composition between the two fractions (the detrital fraction is ∼2–4 units less radiogenic than the authigenic fraction) strongly suggests that congruent leaching of the detrital sediment fraction, either via in-situ chemical weathering at the seafloor and/or during sample processing, does not control temporal variability in our authigenic records spanning MIS 12 and 11 (Fig. S5). The deglacial radiogenic trends in authigenic Pb isotope data from U1302/3 could, however, be the product of seafloor weathering (at U1302/3 or up-stream of it) if it was incongruent (so if the radiogenic phases of the lithogenic fraction of sediments were preferentially leached). In the "Nd model", silicate leaching is more likely to occur during intervals of reduced bottom current speed when the longer benthic exposure time that results allows seawater (and the authigenic phase) to converge toward detrital fraction compositions (e.g., Du et al., 2020). Yet, the orbital-scale evolution of AMOC vigour during the Quaternary (lowest/highest during glacials / terminations and interglacials, e.g., Böhm et al., 2015) is of the wrong sign for Pb remobilization of this type to explain the origin of the radiogenic pulses associated with glacial terminations at Orphan Knoll.

The absence of a major role for seafloor weathering in creating the deglacial authigenic Pb isotope signals at U1302/3 is supported by the presence of a distinct PAAS-normalised mid-REE (MREE) enrichment in our leachate samples that is not observed in the distribution of REE in our detrital samples (Fig. S6; Piper, 1974). Excluding detrital carbonate (H-) layers, the REE signature of most of the MIS 12 and 11 samples (n = 20 out of 29) overlap with that of HH-extracted leachate seawater signals in a cross plot of the REE slope (HREE/LREE) and MREE bulge (MREE/MREE*; Fig. 6). Some of our authigenic data (n = 9 out of 29) encroach on the REE signature of residual detrital sediment fractions (black triangles and black circles with blue outlines in Fig. 6a-b), consistent with incomplete removal of oxides, partial leaching of the detrital component by pore waters in the sediment pile (Blaser et al., 2019) or during sediment processing (Martin et al., 2010). Most of the nine samples with a REE signature that encroaches on that of our detrital sediment fractions correspond to the tail-end of the decay of the authigenic Pb isotope radiogenic signal associated with this transition (see blue circles with black outlines in Fig. 6b that correspond to the authigenic Pb isotope data spanning ∼413–405 ka in panel a). This leaves open the possibility that the duration of this radiogenic signal may be influenced by in-situ weathering of seafloor sediments, albeit this is more likely only for REE and not for Pb (Henderson and Maier-Reimer, 2002). We also discuss the significance of this possibility for our inferences of LIS history during this interglacial in Section 4.3 (below). In any case, the Al/Nd, Al/Th and Al/Pb ratio compositions of the authigenic fraction for all our samples are significantly lower than the Al/Nd, Al/Th and Al/Pb ratios of their detrital counterparts, essentially invariant over the studied time interval, and are closest to those of deep ocean Fe-Mn crusts that represent a pristine seawater signal (Fig. 7). While we acknowledge that our authigenic data may not represent a pristine record of the Pb isotope composition of seawater, we emphasize that being able to prove that they do, is not relevant to the objectives of our study. This is because we are focused on identifying the occurrence in time of the most radiogenic values in the deglacial radiogenic trends in these data as well as the duration of those trends, and not their absolute values. The very distinct isotopic compositions seen in the authigenic and detrital phases and the low Al/Pb of all authigenic samples strongly
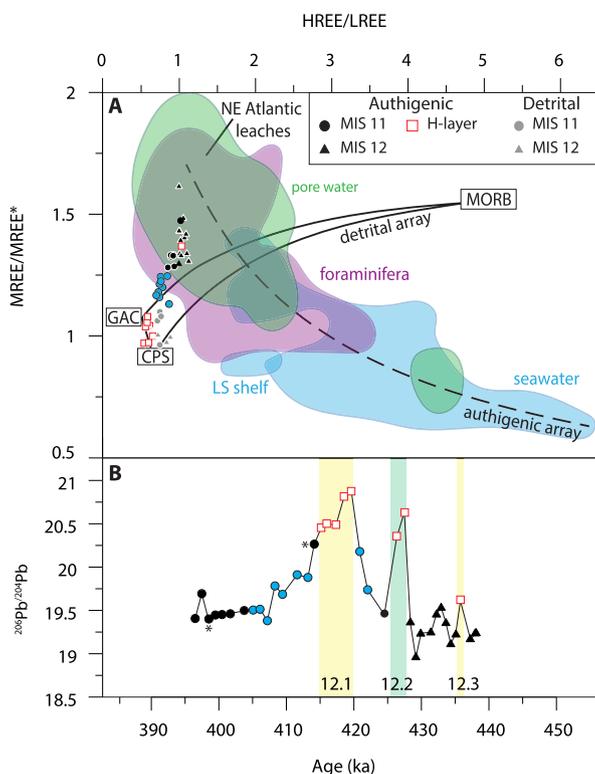
Fig. 6. (**A**) Comparison of PAAS normalised rare earth element (REE) slope (HREE/LREE) and mid-REE bulge (MREE/MREE*) of detrital sediment samples and their authigenic Fe-Mn oxyhydroxides coatings deposited at IODP Site U1302/3 during marine isotope stages (MIS) 12/11 (440–395 ka). (**B**) Corresponding $^{206}Pb/^{204}Pb$ ratios with same symbols shown in (A). Seawater, pore fluids, foraminifera and authigenic phase fields shown are from Blaser et al. (2020; see their Fig. 3 for phase field data sources), defined using bulk foraminiferal REE data from core top to Last Glacial Caribbean, Northwest Atlantic and Equatorial Pacific sediments (purple), seawater data (blue) from the eastern subpolar North Atlantic, equatorial Atlantic, and the Atlantic sector of the Southern Ocean, and pore water data of three sites from the Oregon margin (green). Northeast Atlantic leaches comprise Holocene and LGM data from Blaser et al. (2019), generated with the same leach method used in this study. The curved dashed line defines a potential "authigenic array" following Du et al. (2016). It is defined by mixing of the most HREE enriched seawater included with the most MREE enriched diagenetic ferro-manganese nodule from Pacific Ocean Clarion-Clipperton Fracture Zone (see Blaser et al. (2020) Fig. 3 for data sources). The solid black curved lines define a detrital mixing array between Mid Ocean Ridge Basalts (MORB), Greenland Archean Crust (GAC), and Canadian Precambrian shield cratonic rocks (CPS). Samples with no corresponding REE data are denoted by an asterix (*).

suggests, however, that our authigenic Pb isotope compositions are likely not much different from past dissolved or colloidal signatures at Orphan Knoll.

4.3. What do trends in authigenic Pb isotope records from U1302/3 reveal about Laurentide Ice Sheet retreat during Termination 5?

The relatively unradiogenic values of authigenic Pb isotope data at U1302/3 during MIS 12 (e.g., ~19.6 $^{206}Pb/^{204}Pb$; Fig. 8d-f) reflect LIS suppression of chemical weathering on North America, increased deposition of relatively unradiogenic North American-sourced aeolian dust (Fig. 8g) and a reduction in Labrador Current vigour. The more radiogenic (sometimes Holocene-like) subset of authigenic Pb isotope values that we report for MIS 12 (n = 4 out of 11) may reflect increases in microorganism-mediated chemical weathering of the SP beneath the LIS (Wadham et al., 2010) and solute flux as it shifted from a cold-based to warm-based ice sheet during minor suborbital-scale reductions in its volume/spatial extent (cf. Gutjahr et al., 2014). Regardless, the orbital-scale trend towards more radiogenic values from ~429 ka records an increase in chemical weathering of North American bedrock due to the onset of LIS retreat during T5. Strikingly, the timing that we infer for the onset of LIS retreat based on our records (from ~429.2 ± 7.9 ka, 2σ; Table 1) is highly consistent with the timing of the onset of T5 inferred from the Red Sea sea-level (~430 ka, vertical arrow with grey asterisk in Fig. 5a; Grant et al., 2014) and Chinese Sabo Cave speleothem (~430 ka; Cheng et al., 2012, vertical arrow with red asterisk in Fig. 5a) records, as well as the $^{40}Ar/^{39}Ar$ dated Ital-

ian Palaeo-Tiber River record (437 ± 7 ka, 1σ, vertical arrow with blue asterisk in Fig. 5a; Regattieri et al., 2016).

The collapse of the Hudson Bay Ice Saddle during MIS 11 is not documented in U1302/3 sediments by a red detrital layer (*sense stricto*) as it was during the Eemian (Fig. 5j). We predict that such a layer would be found in cores recovered from locations more proximal to the source (e.g., Hudson Straits/Bay). In the absence of a layer at Site U1302/3, a latest possible age for Hudson Bay Ice Saddle collapse can instead be inferred, through analogy with T1 and T2, from the time at which the most radiogenic values were recorded in deglacial authigenic Pb isotope data from our study site (Fig. 3). In the case of MIS 11, these peak values are, however, partially masked by the deposition of Heinrich-event layer 12.1, ~419.0 ±4.8 ka, 2σ (Fig. 8). We therefore propose that this Heinrich event itself represents or coincided with the collapse of the Hudson Bay Ice Saddle and thus of the LIS during T5. If correct, this demonstrates that any relapse to glacial-style conditions during the intervening insolation minima ~418 ka during MIS 11 (cf. Dickson et al., 2009), was not able to prevent LIS collapse at this time. Our new age for the timing of LIS collapse during MIS 11 cannot be distinguished from the reported timing of sGIS deglaciation during this interglacial (at ~418 ka; Hatfield et al., 2016). Hudson Bay Ice Saddle collapse (Carlson et al., 2008; Dalton et al., 2020; Parker et al., 2022) and sGIS retreat (Colville et al., 2011; Hatfield et al., 2016) also culminated at the same time during the last deglacial (~8.4–8.2 ka; Fig. 5d). During MIS 5e, sGIS retreat continued, however, for ~10 kyr (until ~116 kyr, Fig. 5d; Hatfield

Table 1

Estimates of the timing and duration of key events in the history of LIS deglaciation during three late Pleistocene terminations based on authigenic Pb isotope data from IODP Site U1302/3.

Termination	Onset of LIS retreat (T_o; ka)	±1σ (2σ)	LIS break-up (T_b; ka)[*]	±1σ (2σ)	LIS loss (T_l; ka)[**]	±1σ (2σ)	T_b–T_o (ka)	±1σ (2σ)	T_b–T_l (ka)	±1σ (2σ)
1	19.9	2.4 (3.9)	8.2	1.4 (3.3)	2.6	2.2 (2.2)	11.7	2.8 (5.1)	17.3	2.5 (4.5)
2	134.7	2.2 (4.2)	125.9	2.3 (5.4)	122.1	2.5 (6.8)	8.8	3.2 (6.9)	12.6	3.3 (8.0)
5[***]	(429.2)	3.3 (7.9)	419.0	2.1 (4.7)	407.1	2.1 (4.7)	10.2	4.0 (9.3)	22.1	4.1 (9.2)

[*] LIS break-up is defined as timing of Hudson Bay Ice Saddle collapse as inferred from peak values in Site U1302/3 authigenic Pb isotope data spanning deglacial terminations.

[**] LIS loss is defined as total deglaciation of this ice-sheet as tracked by the return to late Holocene-like values in Site U1302/3 deglacial authigenic Pb isotope data.

[***] The T5 values presented here are based on the U1302/3 authigenic $^{206}Pb/^{204}Pb$ isotope data only; based on $^{207}Pb/^{204}Pb$ isotope data, LIS loss = 413.2 ± 4.2 ka and T_b - T_l = 16.0± 9.2 ka; based on $^{208}Pb/^{204}Pb$ isotope data, LIS loss = 405.0 ± 4.7 ka, and T_b - T_l = 24.2± 9.0 ka.
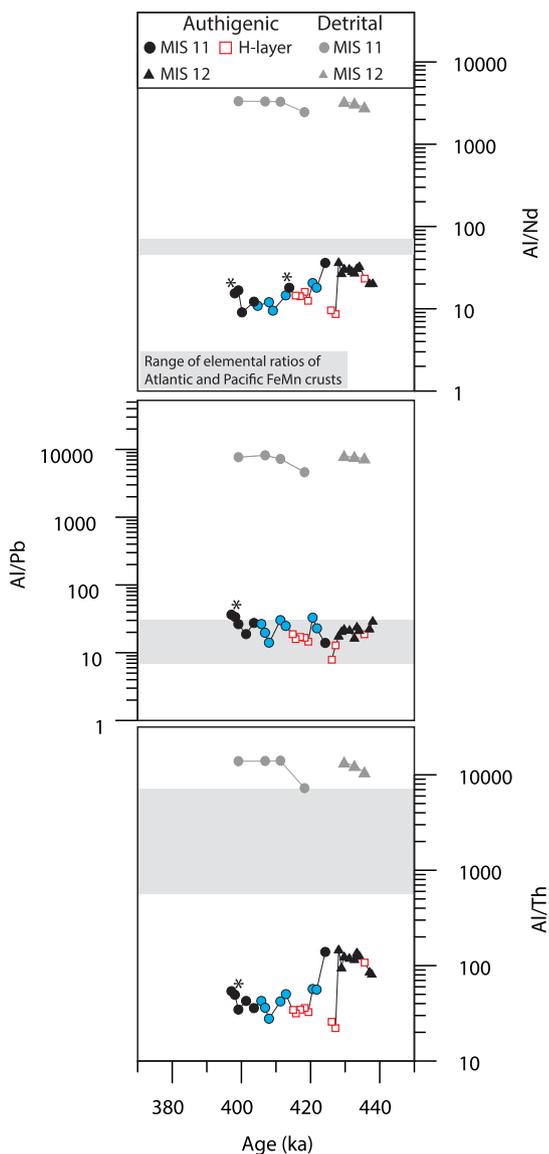

Fig. 7. Elemental ratios of: (A) Al/Nd, (B) Al/Pb and (C) Al/Pb of leachate (black) and detrital sediment (grey) fractions for MIS 12-11 from IODP Site U1302/03. Note the log scale of y-axis. Data symbols correspond with those plotted in Fig. 6. Grey boxes define the range of elemental ratios associated with Atlantic and Pacific Fe-Mn crusts (Hein et al., 1999). Samples with no corresponding PAAS-normalised REE ratio are denoted by an asterisk (*).

et al., 2016) after LIS Hudson Bay Ice Saddle collapse (125.9 ± 5.4 ka, 2σ; Fig. 5).

Atmospheric CO_2 concentrations (Fig. 8k) were above early Holocene peak values (of 265 ppm) from ∼426 ka (Lüthi et al., 2008) and contributed to early and sustained interglacial radiative forcing during MIS 11 for ∼30 kyr from this time (Rohling et al., 2012). The fact that sGIS deglaciation during T5 occurred ∼418 ka, ∼9 kyr before peak summer boreal insolation was crossed during MIS 11 (Fig. 8k) has been used to argue that CO_2 forcing, and not summer boreal insolation, played the leading role in driving ice-sheet retreat during this interglacial (Hatfield et al., 2016). The similar timing for LIS collapse (∼419 ka) inferred here using our new authigenic Pb isotope records may therefore support this notion. We note, though, the time it took for LIS collapse to occur during T5 was not anomalously fast when compared to the history of the same event during T1 (10.2 ± 9.3 kyr (2σ) vs 11.7 ± 5.1 kyr (2σ), respectively; Table 1).

The time from which authigenic Pb isotope data from Orphan Knoll first attained late Holocene-like values (e.g., ∼19.6 $^{206}Pb/^{204}Pb$) provides a marker for the total loss of the LIS during deglaciation (which by analogy to the Holocene represents the time from when glaciation of northeast North America must have been mainly restricted to the Canadian Arctic Archipelago). While this event does not occur at the same time during MIS 11 across our three authigenic Pb isotope records, we can infer from them that LIS deglaciation did not occur earlier than 413.2 ± 4.2 ka (2σ) during T5 (based on our $^{207}Pb/^{204}Pb$ data) or later than 405.0 ± 4.7 ka (2σ, based on our $^{208}Pb/^{204}Pb$ data).

The Pb isotope composition of solute flux associated with increased chemical weathering of an unglaciated southern Greenland has the potential to counteract (or suppress) the radiogenic signal from North America associated with LIS retreat. This is because Greenland's terranes have lower mean Pb isotope ratios in Pb-Pb space than the SP (Fig. 4 and Section 2). Termination of Southern Greenland deglaciation from ∼418 ka (Hatfield et al., 2016), may therefore explain why the decay of the deglacial radiogenic SP-derived signal in our MIS 11 records is diachronous. We note that the timing of LIS deglaciation based on our $^{206}Pb/^{204}Pb$ and $^{208}Pb/^{204}Pb$ data are highly comparable (∼405–407 ka; Fig. 8d, f; Table 1). The $^{207}Pb/^{204}Pb$ isotope ratios are the least diagnostic data for Pb provenance (see Fig. 4). The earlier timing for LIS deglaciation of ∼413 ka that can be inferred from our $^{207}Pb/^{204}Pb$ data may instead also be influenced by the subordinate impact of incongruent weathering on the decay of our T5 radiogenic deglacial signal during MIS 11.

Once the LIS was deglaciated (so by no later than ∼405 ka) the Pb isotope composition of the solute flux from an unglaciated
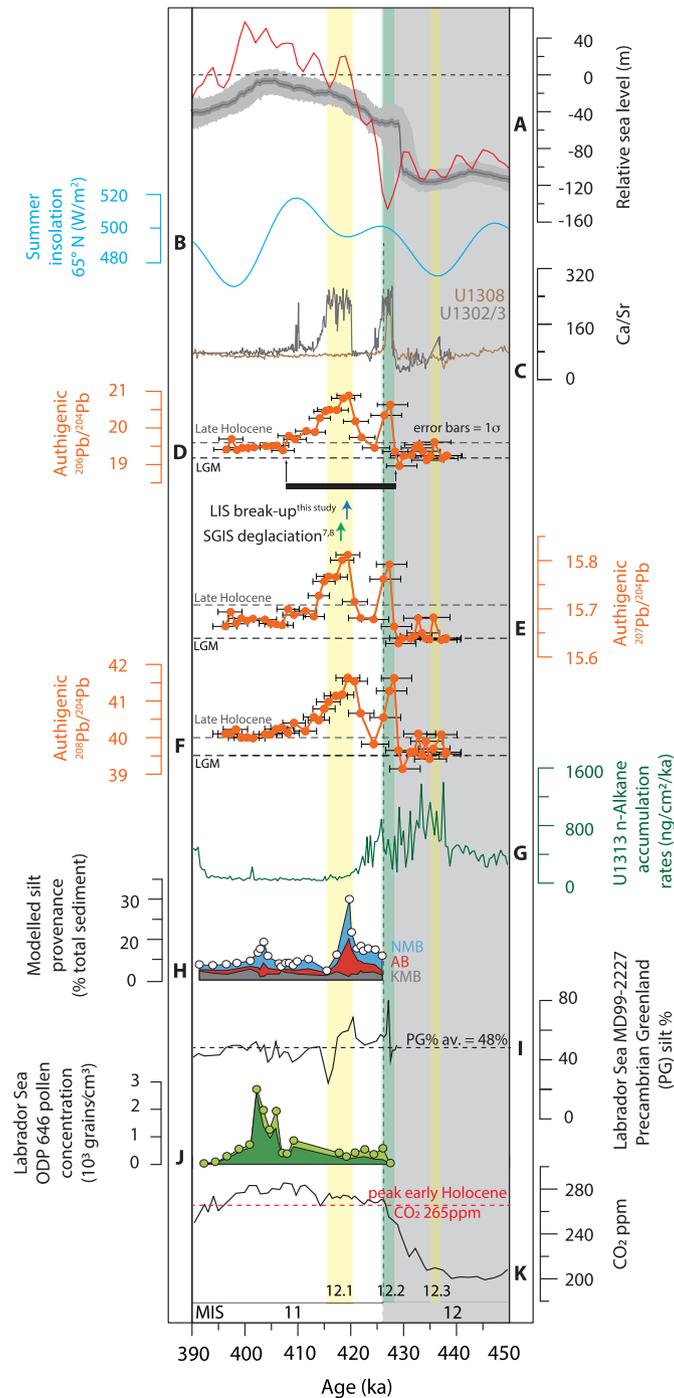
Fig. 8. Palaeoclimate data spanning MIS 12/11 and Termination 5: (**A**) Red Sea relative sea level (RSL) record with 95% probability interval for the RSL data (dark grey envelope) and 95% probability interval for the probability maximum (light grey envelope; Grant et al., 2014). Also shown is a benthic foraminiferal-derived seawater-δ^{18}O-based relative sea-level (RSL) record from ODP Site 1123 (red line; Elderfield et al. (2012); (**B**) Insolation forcing at 21st June 65°N W/m^2; Laskar et al., 2004); (**C**) Orphan Knoll IODP Site U1302/03 and central subpolar North Atlantic IODP Site U1308 (grey and brown, respectively) XRF scanning Ca/Sr ratios (Channell et al., 2012); Pb isotope ratios of authigenic Fe-Mn oxyhydroxides: (**D**) ^{206}Pb/^{204}Pb; (**E**) ^{207}Pb/^{204}Pb; (**F**) ^{208}Pb/^{204}Pb with 1S.D age error bars (T1 and T2, Parker et al., 2022; T5, this study). Late Holocene and LGM values highlighted by horizontal dashed lines; (**G**) Deposition rate of n-alkanes (ng/cm^2/ka) at North Atlantic Site U1313 – a proxy for North American-sourced aeolian deposition (Naafs et al., 2012); (**H**) Inferred provenance of silt deposited at Site MD99-2227 on North Atlantic Eirik Drift – Median solution from 10,000 model runs of a Sr-Nd-Pb isotope mixing model expressed as percent of total sediment derived from the Ketilidian Mobile Belt (KMB; grey), Archean Basement (AB; red) and Nagssugtoqidian Mobile Belt (NMB; blue) terranes. Provenance estimates do not sum to 100% because they do not include clay or sand size fractions (Reyes et al., 2014). (**I**) Modelled contribution of Precambrian Greenland (PG) % silt to sediments deposited at Site MD99-2227 based on a (Mrs/Ms) unmixing model, whereby the ratio of saturation remanence (Mrs) to saturation magnetization (Ms) is used as a proxy for ferrimagnetic grain size with PG silt-sized sediments being magnetically coarser (Mrs/Ms range 0.03–0.1; Hatfield et al., 2016). The average PG mixing of 48% is shown by a dashed line; (**J**) Labrador Sea ODP Site 646 pollen data (De Vernal and Hilliare-Marcel, 2008; core site shown in Fig. 2), showing Picea (dark green) and total (minus Pinus; light green) pollen concentrations. Site 646 data plotted on the MD99-2227 age model following Reyes et al. (2014); (**K**) EPICA Dome C CO$_2$ concentration (ppm) with typical early Holocene peak concentrations of 265ppm (red dashed line; Lüthi et al., 2008 on AICC2012 chronology of Bazin et al., 2013). Horizontal black bars (D) highlight intervals over which we infer enhanced supply of dissolved radiogenic weathered material from the Superior Province craton exposed following Laurentide Ice Sheet retreat in the Hudson Bay region during Termination 5. Blue arrow highlights inferred timing of LIS break up (so Hudson Bay Ice Saddle collapse; this study). Vertical green arrow highlights inferred timing of near-complete deglaciation of southern Greenland Ice Sheet (SGIS; 7 = Hatfield et al., 2016; 8 = Reyes et al., 2014).

Greenland was probably responsible for the even lower than late-Holocene-like $^{206}Pb/^{204}Pb$ and $^{207}Pb/^{204}Pb$ ratios in our authigenic Pb isotope records from this time. We note that sGIS retreat during the Eemian (e.g., Colville et al., 2011), may also be evident in a similar, but shorter-lived, relatively unradiogenic signal for $^{207}Pb/^{204}Pb$ authigenic data spanning MIS 5e between ∼124–119 ka (see Fig. 5e). Regardless, it appears that LIS deglaciation during MIS 11 did not occur prior to the onset of the second of the two precession-paced insolation cycles associated with this interglacial (Fig. 8d–f). If it did not occur until ∼407–405 ka (as suggested by our authigenic $^{206}Pb/^{204}Pb$ and $^{207}Pb/^{204}Pb$ isotope data) then it is likely that ice-mass loss on North America, as driven by insolation forcing, played a central role in the seemingly protracted nature of sea-level rise during T5.

5. Conclusions

We present new high-resolution records of authigenic Fe-Mn oxyhydroxide-derived Pb isotopes from Orphan Knoll IODP Site U1302/3 for MIS 12 and 11 that record the biggest Northern Hemisphere-focused deglaciation event of the Cenozoic, T5, from ∼429 ka. The radiogenic excursions recorded by these records reflect increases in chemical weathering of North American bedrock and solute flux to Orphan Knoll associated with North American Laurentide Ice Sheet (LIS) retreat. To shed new light on the deglaciation history of the LIS during T5, we compared the evolution of orbital-scale radiogenic excursions evident in our new MIS 12/11 records to previously published authigenic Pb isotope datasets from our study site spanning T2 (∼130 ka) and T1 (∼14 ka), all on new age models reported with propagated age uncertainties.

T5 is known as a 'protracted deglaciation' because the full interglacial-glacial transition in mean global sea-level between MIS 12 to 11 was not reached until the second of two weak precession-paced maxima in insolation associated with MIS 11 was crossed, ∼405 ka. Based on our records, we infer LIS retreat during T5 began ∼429.2 ± 7.9 ka (2σ), that Hudson Bay Ice Saddle collapse (as tracked by peak radiogenic values in our deglacial U1302/3 authigenic Pb isotope data) occurred at 419.0 ± 4.7 ka (2σ), and that its full deglaciation occurred by no later than 405.0 ± 4.7 ka (2σ). Our new records allow us to infer that LIS deglaciation likely occurred over a much longer (∼22–24 kyr) timescale than it did during T2 (∼13 kyr) and T1 (∼17 kyr), implying that the protracted nature of sea-level rise during MIS 11 was strongly influenced by the retreat history of the LIS and the underlying boreal summer insolation rise pacing it.

Our findings also provide important new constraints on the deglacial histories of Northern Hemisphere ice-sheets that could be used by GIA modellers to improve the accuracy of estimates of sea-level highstands during, e.g., MIS 11 (e.g., Raymo and Mitrovica, 2012). Our inference that the relative timings of North American and southern Greenland deglaciation is not fixed between one interglacial and the next requires confirmation through future refinements of age-model control for Orphan Knoll and Eirik Drift records. If correct, it does, however, highlight that it may be misleading to use the well constrained history of regional ice-sheet deglaciation during T1, as reconstructed for, e.g., the ICE-5G ice model of the LGC (Peltier, 2004), as a template in GIA modelling for the evolution of ice-sheet geometries during older late Pleistocene terminations.

CRediT authorship contribution statement

Rebecca L. Parker: Formal analysis, Funding acquisition, Investigation, Methodology, Writing – original draft, Writing – review & editing. **Gavin L. Foster:** Conceptualization, Resources, Writing – original draft, Writing – review & editing, Formal analysis, Funding acquisition. **Marcus Gutjahr:** Formal analysis, Methodology, Writing – original draft, Writing – review & editing. **Paul A. Wilson:** Funding acquisition, Resources, Writing – original draft, Writing – review & editing. **Stephen P. Obrochta:** Methodology. **Nathalie Fagel:** Writing – original draft, Writing – review & editing. **Matthew J. Cooper:** Methodology, Writing – original draft, Writing – review & editing. **Agnes Michalik:** Methodology, Writing – original draft, Writing – review & editing. **James A. Milton:** Methodology, Writing – original draft, Writing – review & editing. **Ian Bailey:** Conceptualization, Formal analysis, Investigation, Methodology, Supervision, Writing – original draft, Writing – review & editing.

Declaration of competing interest

The authors declare that they have no known competing financial interests or personal relationships that could have appeared to influence the work reported in this paper.

Data availability

All IODP Site U1302/3 data used in this study are available in this paper's Supplementary data file.

Appendix A. Supplementary material

Supplementary material related to this article can be found online at https://doi.org/10.1016/j.epsl.2023.118286.

References

Abbott, A.N., Löhr, S.C., Payne, A., Kumar, H., Du, J., 2022. Widespread lithogenic control of marine authigenic neodymium isotope records? Implications for paleoceanographic reconstructions. Geochim. Cosmochim. Acta 319, 318–336. https://doi.org/10.1016/j.gca.2021.11.021.

Baker, J., Peate, D., Waight, T., Meyzen, C., 2004. Pb isotopic analysis of standards and samples using a 207Pb/204Pb double spike and thallium to correct for mass bias with a double-focusing MC-ICP-MS. Chem. Geol. 211 (3–4), 275–303.

Barber, D.C., Dyke, A., Hillaire-Marcel, C., Jennings, A.E., Andrews, J.T.A., Kerwin, M., Bilodeau, W.G., McNeely, R., Southon, J., Morehead, M.D., Gagnon, J.-M., 1999. Forcing of the cold event 8,200 years ago by catastrophic drainage of Laurentide lakes. Nature 400, 344–348. https://doi.org/10.1038/22504.

Barker, S., Knorr, G., Conn, S., Lordsmith, S., Newman, D., Thornalley, D., 2019. Early interglacial legacy of deglacial climate instability. Paleoceanogr. Paleoclimatol. 34, 1455–1475. https://doi.org/10.1029/2019PA003661.

Barker, S., Zhang, X., Jonkers, L., Lordsmith, S., Conn, S., Knorr, G., 2021. Strengthening Atlantic inflow across the mid-Pleistocene transition. Paleoceanogr. Paleoclimatol. 36, e2020PA004200. https://doi.org/10.1029/2020PA004200.

Bazin, L., et al., 2013. An optimized multi-proxy, multi-site Antarctic ice and gas orbital chronology (AICC2012): 120–800 ka. Clim. Past 9, 1715–1731. https://doi.org/10.5194/cp-9-1715-2013.

Blake-Mizen, K.R., Hatfield, R.G., Stoner, J.S., Carlson, A.E., Xuan, C., Walczak, M.H., Lawrence, K.T., Channell, J.E.T., Bailey, I., 2019. Southern Greenland glaciation and western boundary undercurrent evolution recorded on Eirik Drift during the late Pliocene intensification of Northern Hemisphere glaciation. Quat. Sci. Rev. 209, 40–51. https://doi.org/10.1016/j.quascirev.2019.01.015.

Blaser, P., Lippold, J., Gutjahr, M., Frank, N., Link, J.M., Frank, M., 2016. Extracting foraminiferal seawater Nd isotope signatures from bulk deep sea sediment by chemical leaching. Chem. Geol. 439, 189–204. https://doi.org/10.1016/j.chemgeo.2016.06.024.

Blaser, P., Pöppelmeier, F., Schulz, H., Gutjahr, M., Frank, M., Lippold, J., Heinrich, H., Link, J.M., Hoffmann, J., Szidat, S., Frank, N., 2019. The resilience and sensitivity of Northeast Atlantic deep water εNd to overprinting by detrital fluxes over the past 30,000 years. Geochim. Cosmochim. Acta 245, 79–97. https://doi.org/10.1016/j.gca.2018.10.018.

Blaser, P., Gutjahr, M., Pöppelmeier, F., Frank, M., Kaboth-Bahr, S., Lippold, J., 2020. Labrador Sea bottom water provenance and REE exchange during the past 35,000 years. Earth Planet. Sci. Lett. 542, 116299. https://doi.org/10.1016/j.epsl.2020.116299.

Böhm, E., Lippold, J., Gutjahr, M., Frank, M., Blaser, P., Antz, B., Fohlmeister, J., Frank, N., Andersen, M.B., Deininger, M., 2015. Strong and deep Atlantic meridional overturning circulation during the last glacial cycle. Nature 517, 73–79. https://doi.org/10.1038/nature14059.

Brouard, E., Roy, M., Godbout, P-M., Veillette, J.J., 2021. A framework for the timing of the final meltwater outbursts from glacial Lake Agassiz-Ojibway. Quat. Sci. Rev. 274, 107269. https://doi.org/10.1016/j.quascirev.2021.107269.

Chen, M., Carrasco, G., Zhao, N., Wang, X., Lee, J.N., Tanzil, J.T.I., Annammala, K.A., Poh, S.C., Lauro, F.M., Ziegler, A.D., Duangnamon, D., Boyel, E.A., 2023. Boundary exchange completes the marine Pb cycle jigsaw. Proc. Natl. Acad. Sci. 120 (6), e2213163120. https://doi.org/10.1073/pnas.2213163120.

Cheng, H., Zhang, P., Spötl, C., Edwards, R., Cai, Y., Zhang, D., Sang, W., Tan, M., An, Z., 2012. The climatic cyclicity in semiarid-arid Central Asia over the past 500 000 years. Geophys. Res. Lett. 39, 1705. https://doi.org/10.1029/2011GL050202.

Colville, E.J., Carlson, A.E., Beard, B.L., Hatfield, R.G., Stoner, J.S., Reyes, A.V., Ullman, D.J., 2011. Sr–Nd–Pb isotope evidence for ice-sheet presence on southern Greenland during the last interglacial. Science 333, 620–623. https://doi.org/10.1126/science.1204673.

Carlson, A.E., Stoner, J.S., Donnelly, J.P., Hillaire-Marcel, C., 2008. Response of the southern Greenland Ice Sheet during the last two deglaciations. Geology 36, 359–362. https://doi.org/10.1130/G24519A.1.

Channell, J.E.T., Kanarnatsu, T., Sato, T., Stein, R., Alvarez Zarikian, C.A., Malone, M.J., 2006. Sites U1302 and U1303. In: Proceedings of the IODP, Volume 303/306, College Station TX (Integrated Ocean Drilling Program Management).

Channell, J.E.T., Hodell, D.A., Romero, O., Hillaire-Marcel, C., de Vernal, A., Stoner, J.S., et al., 2012. A 750-kyr detrital-layer stratigraphy for the North Atlantic (IODP Sites U1302-U1303, Orphan Knoll, Labrador Sea). Earth Planet. Sci. Lett. 317–318, 218–230. https://doi.org/10.1016/j.epsl.2011.11.029.

Crocket, K.C., Vance, D., Foster, G.L., Richards, D.A., Tranter, M., 2012. Continental weathering fluxes during the last glacial/interglacial cycle: insights from the marine sedimentary Pb isotope record at Orphan Knoll, NW Atlantic. Quat. Sci. Rev. 30, 89–99. https://doi.org/10.1016/j.quascirev.2012.02.004.

Dalton, A.S., Margold, M., Stokes, C.R., Tarasov, L., Dyke, A.S., Adams, R.S., et al., 2020. An updated radiocarbon-based ice margin chronology for the last deglaciation of the North American Ice Sheet Complex. Quat. Sci. Rev. 234. https://doi.org/10.1016/j.quascirev.2020.106223.

Dausmann, V., Gutjahr, M., Frank, M., Kouzmanov, K., Schaltegger, U., 2019. Experimental evidence for mineral-controlled release of radiogenic Nd, Hf and Pb isotopes from granitic rocks during progressive chemical weathering. Chem. Geol. 507, 64–84. https://doi.org/10.1016/j.chemgeo.2018.12.024.

De Vernal, A., Hiliare-Marcel, C., 2008. Natural variability of Greenland climate, vegetation, and ice volume during the past million years. Science 320, 1622–1625. https://doi.org/10.1126/science.1153929.

Dendy, S., Austermann, J., Creveling, J.R., Mitrovica, J.X., 2017. Sensitivity of last interglacial sea-level high stands to ice sheet configuration during Marine Isotope Stage 6. Quat. Sci. Rev. 171, 234–244. https://doi.org/10.1016/j.quascirev.2017.06.013.

Dickson, A.J., Beer, C.J., Dempsey, C., Maslin, M.A., Bendle, J.A., McClymont, E.L., Pancost, R.D., 2009. Oceanic forcing of the Marine Isotope Stage 11 interglacial. Nat. Geosci. 2, 428–433. https://doi.org/10.1038/ngeo527.

Du, J., Haley, B.A., Mix, A.C., 2016. Neodymium isotopes in authigenic phases, bottom waters and detrital sediments in the Gulf of Alaska and their implications for paleo-circulation reconstruction. Geochim. Cosmochim. Acta 193, 14–35. https://doi.org/10.1016/j.gca.2016.08.005.

Du, J., Haley, B.A., Mix, A.C., 2020. Evolution of the global overturning circulation since the last glacial maximum based on marine authigenic neodymium isotopes. Quat. Sci. Rev. 241, 106396. https://doi.org/10.1016/j.quascirev.2020.106396.

Dyer, B., Austermann, J., D'Andrea, W.J., Crell, R.C., Sandstrom, M.R., Cashman, M., Rovere, A., Raymo, M.E., 2021. Sea-level trends across the Bahamas constrain peak last interglacial ice melt. Proc. Natl. Acad. Sci. 118 (33), e202689118. https://doi.org/10.1073/pnas.2026839118.

Dyke, A.S., Andrews, J.T., Clark, P.U., England, J.H., Miller, G.H., Shaw, J., Veillette, J.J., 2002. The Laurentide and Innuitian ice sheets during the last glacial maximum. Quat. Sci. Rev. 21, 9–31.

Dutton, A., Carlson, A.E., Long, A.J., Milne, G.A., Clark, P.U., DeConto, R., Horton, B.P., Rahmstorf, S., Raymo, M.E., 2015. Sea-level rise due to polar ice-sheet mass loss during past warm periods. Science 349. https://doi.org/10.1126/science.aaa4019.

Elderfield, H., Ferretti, P., Greaves, M., Crowhurst, S., McCave, I.N., Hodell, D., Piotrowski, A.M., 2012. Evolution of ocean temperature and ice volume through the mid-Pleistocene climate transition. Science 337, 704–709. https://doi.org/10.1126/science.12212.

Expedition 303 Scientists, 2006. Site U1308. In: Channell, J.E.T., et al. (Eds.), North Atlantic Climate, Proc. Integr. Ocean Drill. Program 303. https://doi.org/10.2204/iodp.proc.303306.108.2006.

Fagel, N., Innocent, C., Gariepy, C., Hillaire-Marcel, C., 2002. Sources of Labrador Sea sediments since the last glacial maximum inferred from Nd-Pb isotopes. Geochem. Cosmochim. Acta 66 (14), 2569–2581. https://doi.org/10.1016/50016-7037(02)00866-9.

Grant, K.M., Rohling, E.J., Ramsey, C.B., Cheng, H., Edwards, R.L., Florindo, F., Heslop, D., Marra, F., Roberts, A.P., Tamisiea, M.E., Williams, F., 2014. Sea-level variability over five glacial cycles. Nat. Commun. 5, 5076. https://doi.org/10.1038/ncomms6076.

Gutjahr, M., Frank, M., Stirling, C.H., Klemm, V., van de Flierdt, T., Halliday, A.N., 2007. Reliable extraction of a deepwater trace metal isotope signal from Fe-Mn oxyhydroxide coatings of marine sediments. Chem. Geol. 242 (3–4), 351–370. https://doi.org/10.1016/j.chemgeo.2007.03.021.

Gutjahr, M., Frank, M., Lippold, J., Halliday, A.N., 2014. Peak Last Glacial weathering intensity on the North American continent recorded by the authigenic Hf isotope composition of North Atlantic deep-sea sediments. Quat. Sci. Rev. 99, 97–111. https://doi.org/10.1016/j.quascirev.2014.06.022.

Haley, B.A., Klinkhammer, G.P., McManus, J., 2004. Rare Earth elements in pore waters of marine sediments. Geochim. Cosmochim. Acta 68, 1265–1279. https://doi.org/10.1016/j.gca.2003.09.012.

Hatfield, R.G., Reyes, A.V., Stoner, J.S., Carlson, A.E., Bard, B.L., Winsor, K., Welke, B., 2016. Interglacial responses of the Southern Greenland ice sheet over the last 430,000 years determined using particle-size specific magnetic and isotopic tracers. Earth Planet. Sci. Lett. 454, 225–236. https://doi.org/10.1016/j.epsl.2016.09.014.

Hein, J.R., Koschinsky, A., Bau, M., Manheim, F.T., Kang, J.-K., Roberts, L., 1999. Cobalt-rich ferromanganese crusts in the Pacific. In: Cronan, D.S. (Ed.), Handbook of Marine Mineral Deposits. CRC Press, pp. 239–279.

Henderson, G.M., Maier-Reimer, E., 2002. Advection and removal of ^{210}Pb and stable Pb isotopes in the oceans: a general circulation model study. Geochim. Cosmochim. Acta 66, 257–272. https://doi.org/10.1016/S0016-7037(01)00779-7.

Hillaire-Marcel, C., de Vernal, A., McKay, J., 2011. Foraminifer isotope study of the Pleistocene Labrador Sea, northwest North Atlantic (IODP Sites 1302/03 and 1305), with emphasis on paleoceanographical differences between its "inner" and "outer" basins. Mar. Geol. 279, 188–198.

Hodell, D.A., Channell, J.E.T., Curtis, J.H., Romero, O.E., Röhl, U., 2008. Onset of "Hudson Strait" Heinrich events in the eastern North Atlantic at the end of the middle Pleistocene transition (<640 ka)? Paleoceanography 23, PA4218. https://doi.org/10.1029/2008PA001591.

Jennings, A.E., Andrews, J.T., Pearce, C., Wilson, L., Ólfasdótttir, S., 2015. Detrital carbonate peaks on the Labrador Shelf, a 13 to 7 ka template for freshwater forcing from the Hudson Strait outlet of the Laurentide Ice Sheet into the subpolar gyre. Quat. Sci. Rev. 107, 62–80. https://doi.org/10.1016/j.quascirev.2014.10.022.

Kurzweil, F., Gutjahr, M., Vance, D., Keigwin, L., 2010. Authigenic Pb isotopes from the Laurentian Fan: changes in chemical weathering and patterns of North American freshwater runoff during the last deglaciation. Earth Planet. Sci. Lett. 299, 458–465. https://doi.org/10.1016/j.epsl.2010.09.031.

Lajeunesse, P., St-Onge, G., 2008. The subglacial origin of the Lake Agassiz-Ojibway final outburst flood. Nat. Geosci. 1, 184–187. https://doi.org/10.1038/ngeo130.

Laskar, J., Robutel, P., Joutel, F., Gastineau, M., Correia, A.C.M., Levrard, B., 2004. A long-term numerical solution for the insolation quantities of the Earth. Astron. Astrophys. 428, 261–285. https://doi.org/10.1051/0004-6361:20041335.

Lisiecki, L.E., Raymo, M.E., 2005. A Pliocene-Pleistocene stack of 57 globally distributed benthic δ^{18}O records. Paleoceanography 20 (1), 1–17. https://doi.org/10.1029/2004PA001071.

Lochte, A.A., Repschläger, J., Kienast, M., Garbe-Schönberg, D., Andersen, N., Hamann, C., Schneider, R., 2019. Labrador Sea freshening at 8.5 ka BP caused by Hudson Bay Ice Saddle collapse. Nat. Commun. 10, 5869. https://doi.org/10.1038/s41467-019-08408-6.

Lougheed, B.C., Obrochta, S.P., 2019. A rapid, deterministic age-depth modeling routine for geological sequences with inherent depth uncertainty. Paleoceanogr. Paleoclimatol. 34, 122–133. https://doi.org/10.1029/2018PA003457.

Loulergue, L., Schilt, A., Spahni, R., Masson-Delmotte, V., Blunier, T., Lemieux, B., Chappellaz, J., 2008. Orbital and millennial-scale features of atmospheric CH$_4$ over the past 800,000 years. Nature 453, 383–386. https://doi.org/10.1038/nature06950.

Loutre, M.F., Berger, A., 2003. Marine Isotope Stage 11 as an analogue for the present interglacial. Glob. Planet. Change 36, 209–217. https://doi.org/10.1016/S0921-8181(02)00186-8.

Lüthi, D., Le Floch, M., Bereiter, B., Blunier, T., Barnola, J.-M., Siegenthaler, U., Raynaud, D., Jouzel, J., Fischer, H., Kawamura, K., Stocker, T.F., 2008. High-resolution carbon dioxide concentration record 650,000–800,000 years before present. Nature 453, 379–382. https://doi.org/10.1038/nature06949.

Margold, M., Stokes, C.R., Clark, C.D., 2018. Reconciling records of ice streaming and ice margin retreat to produce a palaeogeographic reconstruction of the

deglaciation of the Laurentide Ice Sheet. Quat. Sci. Rev. 189, 1–30. https://doi.org/10.1016/j.quascirev.2018.03.013.

Martin, E.E., Blair, S.W., Kamenov, G.D., Scher, H.D., Bourbon, E., Basak, C., Newkirk, D.N., 2010. Extraction of Nd isotopes from bulk deep sea sediments for paleoceanographic studies on Cenozoic time scales. Chem. Geol. 269, 414–443. https://doi.org/10.1016/j.chemgeo.2009.10.016.

McManus, J., Oppo, D., Cullen, J., Healey, S., 2003. Marine Isotope Stage 11 (MIS 11): Analog for Holocene and Future Climate? In Geophysical Monograph Series, vol. 137. American Geophysical Union, Washington, DC, pp. 69–85.

Naafs, B.D.A., Hefter, J., Acton, G., Haug, G.H., Martínez-Garcia, A., Pancost, R., Stein, R., 2012. Strengthening of North American dust sources during the late Pliocene (2.7 Ma). Earth Planet. Sci. Lett. 317–318, 8–19. https://doi.org/10.1016/j.epsl.2011.11.02.

Natural Resources Canada, 2006. Atlas of Canada Watershed Framework. https://www.nrcan.gc.ca/maps-tools-publications/tools/geodetic-reference-systems/water/16888. (Accessed 10 June 2021).

Nicholl, J.A.L., Hodell, D.A., Naafs, B.D.A., Hillaire-Marcel, C., Channell, J.E.T., Romero, O.E., 2012. A Laurentide outburst flooding event during the last interglacial period. Nat. Geosci. 5, 901–904. https://doi.org/10.1038/NGEO1622.

Parker, R.L., Foster, G.L., Gutjahr, M., Wilson, P.A., Littler, K.L., Cooper, M.J., et al., 2022. Laurentide Ice Sheet extent over the last 130 thousand years traced by the Pb isotope signature of weathering inputs to the Labrador Sea. Quat. Sci. Rev. 287, 107564. https://doi.org/10.1016/2022.107564.

Peltier, W.R., 2004. Global Glacial Isostasy and the Surface of the Ice-Age Earth: The ICE-5G (VM2) Model and GRACE. Annu. Rev. Earth Planet. Sci. 32, 111–149. https://doi.org/10.1146/annurev.earth.32.082503.144359.

Piper, D.Z., 1974. Rare Earth elements in the sedimentary cycle: a summary. Chem. Geol. 14, 285–304. https://doi.org/10.1016/0009-2541(74)90066-7.

Pöppelmeier, F., Lippold, J., Blaser, P., Gutjahr, M., Frank, M., 2022. Neodymium isotopes as a paleo-water mass tracer: a model-data reassessment. Quat. Sci. Rev. 279, 107404. https://doi.org/10.1016/j.quascirev.2022.107404.

Regattieri, E., Giaccio, B., Galli, P., Nomade, S., Peronace, E., Messina, P., Sposato, A., Boschi, C., Gemelli, M., 2016. A multi-proxy record of MIS 11–12 deglaciation and glacial MIS 12 instability from the Sulmona basin (central Italy). Quat. Sci. Rev. 132, 129–145. https://doi.org/10.1016/j.quascirev.2015.11.015.

Raymo, M.E., 1997. The timing of major climate terminations. Paleoceanography 12 (4), 577–585. https://doi.org/10.1029/97PA01169.

Raymo, M.E., Mitrovica, J.X., 2012. Collapse of polar ice sheets during the stage 11 interglacial. Nature 483, 453–456. https://doi.org/10.1038/nature10891.

Reyes, A.V., et al., 2014. South Greenland ice-sheet collapse during Marine Isotope Stage 11. Nature 510, 525–528. https://doi.org/10.1038/nature13456.

Rohling, E.J., Braun, K., Grant, K., Kucera, M., Roberts, A.P., Siddall, M., Trommer, G., 2010. Comparison between Holocene and Marine Isotope Stage-11 sea-level his-

tories. Earth Planet. Sci. Lett. 291, 97–105. https://doi.org/10.1016/j.epsl.2009.12.054.

Rohling, E.J., Medina-Elizalde, M., Shepherd, J.G., Siddall, M., Stanford, J.D., 2012. Sea surface and high-latitude temperature sensitivity to radiative forcing of climate over several glacial cycles. J. Climate 25, 1635–1656. https://doi.org/10.1175/2011JCLI4078.1.

Strelow, F.W.E., 1978. Distribution coefficients and anion-exchange behavior of some elements in hydrobromic nitric acid mixtures. Anal. Chem. 50 (9), 1359–1361. https://doi.org/10.1021/ac50031a041.

Süfke, F., Gutjahr, M., Gilli, A., Anselmetti, F.S., Glur, L., Eisenhauer, A., 2019. Early stage weathering systematics of Pb and Nd isotopes derived from a high-Alpine Holocene lake sediment record. Chem. Geol. 507, 42–53. https://doi.org/10.1016/j.chemgeo.2018.12.026.

Süfke, F., Gutjahr, M., Keigwin, L.D., Reilly, B., Giosan, L., Lippold, J., 2022. Arctic drainage of Laurentide Ice Sheet meltwater throughout the past 14,700 years. Commun. Earth Environ. 3, 98. https://doi.org/10.1038/s43247-022-00428-3.s.

Taylor, R.N., Ishizuka, O., Michalik, A., Milton, J.A., Croudace, I.W., 2015. Evaluating the precision of Pb isotope measurement by mass spectrometry. J. Anal. At. Spectrom. 30, 198–213. https://doi.org/10.1039/C4JA00279B.

Taylor, S.R., McLennan, S.M., 1985. The Continental Crust: Its Composition and Evolution. Blackwell, Oxford. 312 pp.

Toucanne, S., Zaragosi, S., Bourillet, J.F., Gibbard, P.L., Eynaud, F., Giraudeau, J., Turon, J.L., Cremer, M., Cortijo, E., Martinez, P., Rossignol, L., 2009. A 1.2 Ma record of glaciation and fluvial discharge from the West European Atlantic margin. Quat. Sci. Rev. 28 (25–26), 2974–2981. https://doi.org/10.1016/j.quascirev.2009.08.003.

Wadham, J.L., Tranter, M., Skidmore, M., Hodson, A.J., Priscu, J., Lyons, W.B., Sharp, M., Wynn, P., Jackson, M., 2010. Biogeochemical weathering under ice: size matters. Glob. Biogeochem. Cycles 24, GB3025. https://doi.org/10.1029/2009GB003688.

White, L.E., Bailey, I., Foster, G.L., Georgina, A., Kelley, S.P., Andrews, J.T., Hogan, K., Dowdeswell, J.A., Storey, C.D., 2016. Tracking the provenance of Greenland-sourced, Holocene aged individual sand-sized ice-rafted debris using the Pb-isotope composition of feldspars and $^{40}Ar/^{39}Ar$ ages of hornblendes. Earth Planet. Sci. Lett. 433, 192–203. https://doi.org/10.1016/j.epsl.2015.10.054.

Wilson, D.J., Bertram, R.A., Needham, E.F., van de Flierdt, T., Welsh, K.J., McKay, R.M., Mazumder, A., Riesselman, C.R., Jimenez-Espejo, F.J., Escutia, C., 2018. Ice loss from the East Antarctic Ice Sheet during late Pleistocene interglacials. Nature 561, 383–386. https://doi.org/10.1038/s41586-018-0501-8.

Xuan, C., Channell, J.E.T., Hodell, D.A., 2016. Quaternary magnetic and oxygen isotope stratigraphy in diatom-rich sediments of the southern Gardar Drift (IODP Site U1304, North Atlantic). Quat. Sci. Rev. 142, 74–89. https://doi.org/10.1016/j.quascirev.2016.04.010.